Supplementary Information (SI) for Chemical Science.
This journal is © The Royal Society of Chemistry 2026

Supporting Information

Continually band-tunable bismuth oxyhalides $BiOBr_{1-x}I_x$ as O_2-evolving photocatalysts for visible-light-driven Z-scheme water splitting

Hajime Suzuki,[a,b,] Akitoshi Nakamura,[a] Miyuki Ikeda,[a] Toshiki Abe,[a] Yuuki Iida,[a] Osamu Tomita,[a] Masanobu Higashi,[a] Shunsuke Nozawa, [c] Akinori Saeki,[d] and Ryu Abe [a,*]*

[a] Department of Energy and Hydrocarbon Chemistry, Graduate School of Engineering, Kyoto University, Katsura, Nishikyo-ku, Kyoto 615-8510, Japan

[b] Precursory Research for Embryonic Science and Technology (PRESTO), Japan Science and Technology Agency (JST), 4-1-8 Honcho, Kawaguchi, Saitama 332-0012, Japan

[c] Photon Factory (PF), Institute of Materials Structure Science (IMSS), High Energy Accelerator Research Organization (KEK), Tsukuba, Ibaraki 305-0801, Japan

[d] Department of Applied Chemistry, Graduate School of Engineering, The University of Osaka, 2-1 Yamadaoka, Suita, Osaka 565-0871, Japan

AUTHOR INFORMATION

Corresponding Author

* suzuki.hajime.7x@kyoto-u.ac.jp (H. S.)

* ryu-abe@scl.kyoto-u.ac.jp (R. A.)

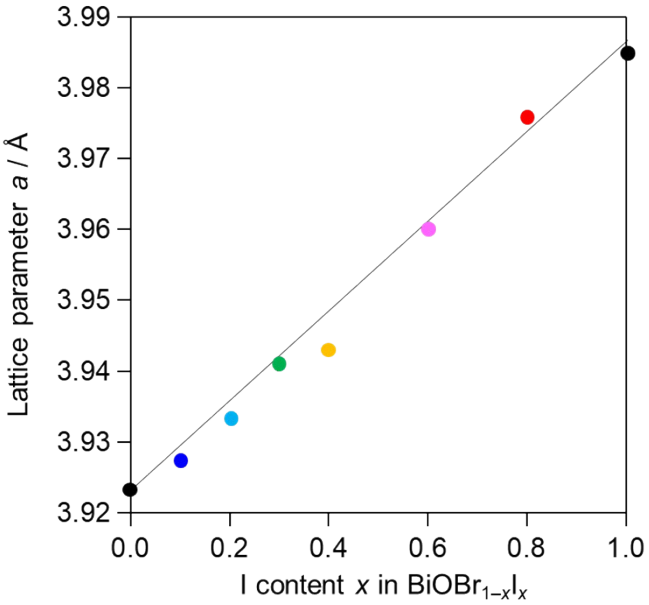

Figure S1. Lattice parameter *a* of the $BiOBr_{1-x}I_x$ samples (x = 0–1) determined from the XRD patterns.

Table S1. EDX-determined I/(Br + I) and I/Bi ratios of $BiOBr_{1-x}I_x$ solid solutions.

x	I/(Br+I)	I/Bi
0.1	0.11	0.11
0.2	0.19	0.19
0.3	0.26	0.26
0.4	0.38	0.40
0.6	0.57	0.62
0.8	0.78	0.77

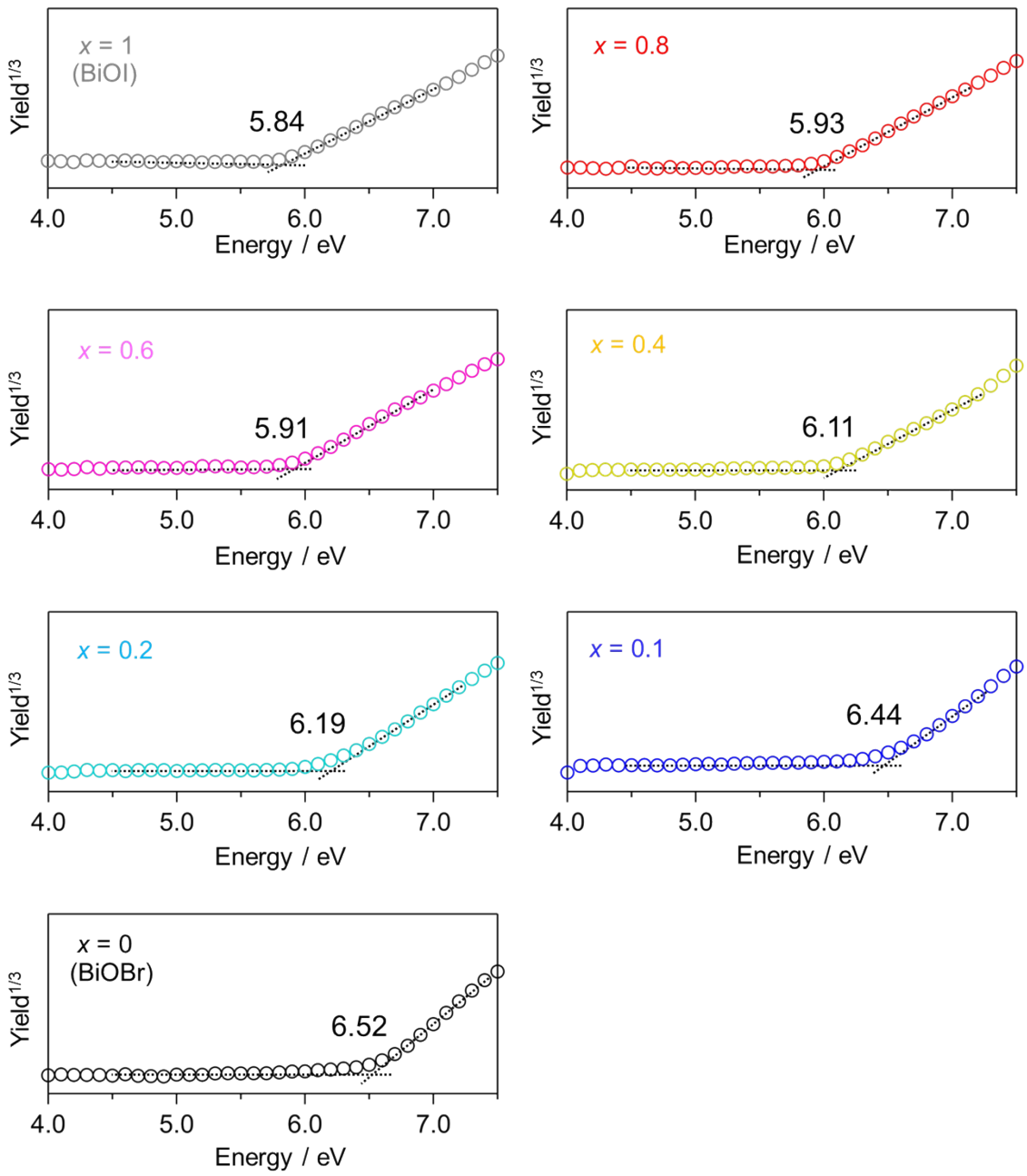

Figure S2. Photoelectron yield spectroscopy (PYS) spectra of $BiOBr_{1-x}I_x$ samples (x = 0–1).

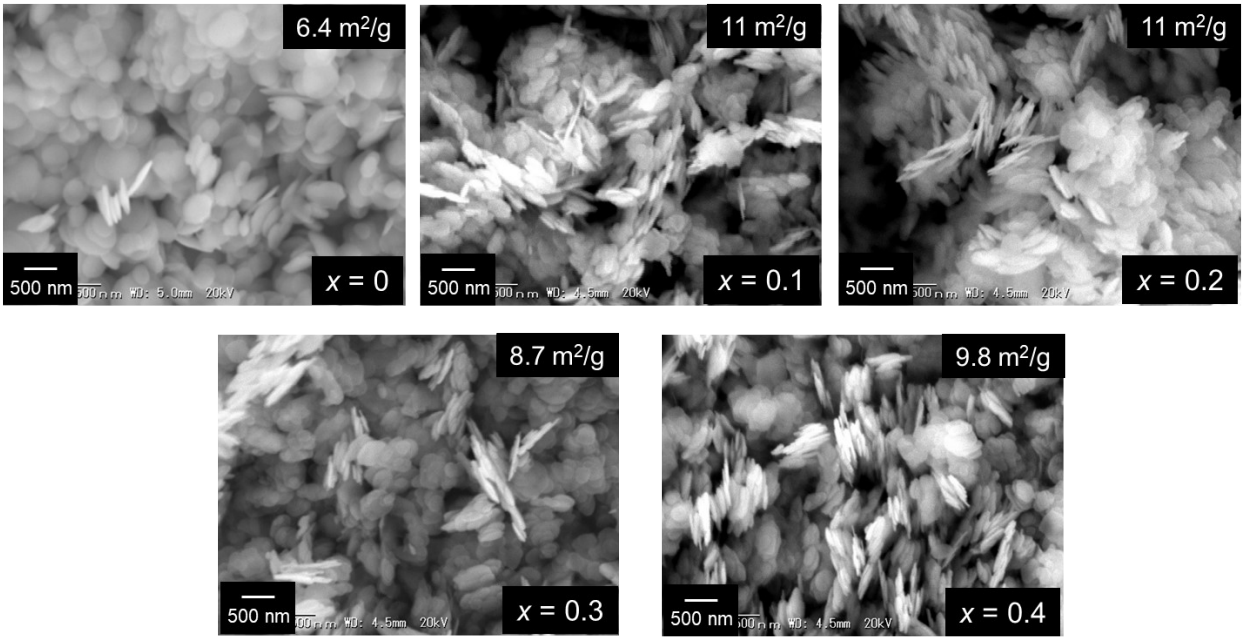

Figure S3. SEM images of representative $BiOBr_{1-x}I_x$ samples (x = 0–0.4).

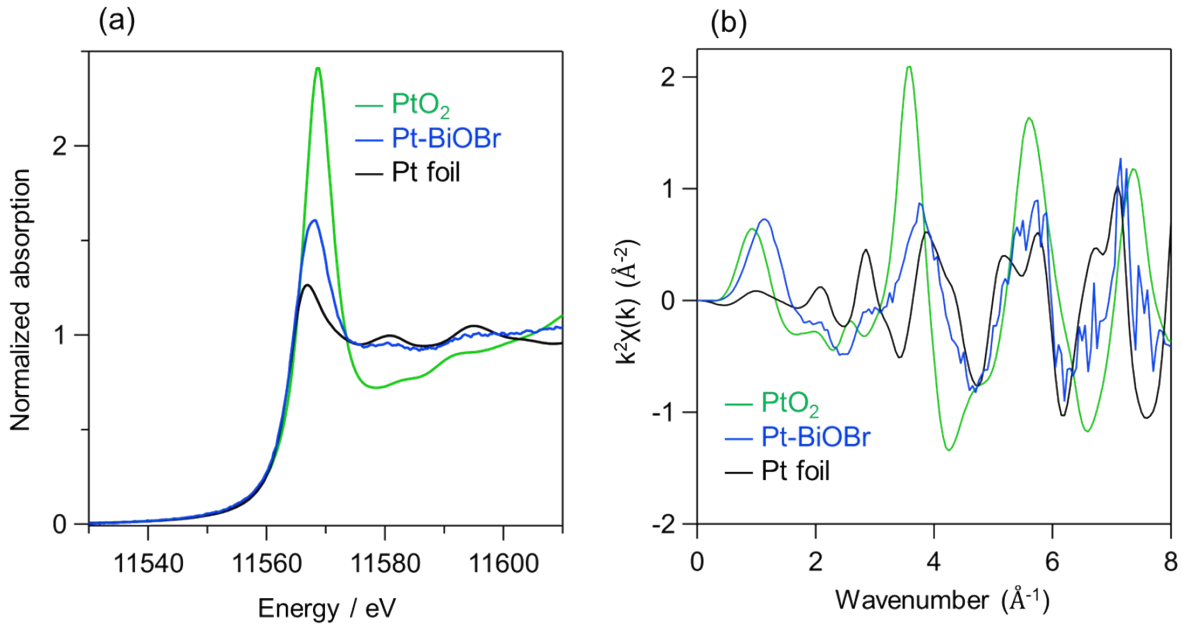

Figure S4. (a) Pt L_3-edge XANES spectrum and (b) EXAFS $k^2\chi(k)$ function for Pt-BiOBr, along with those of Pt foil and PtO_2 as references.

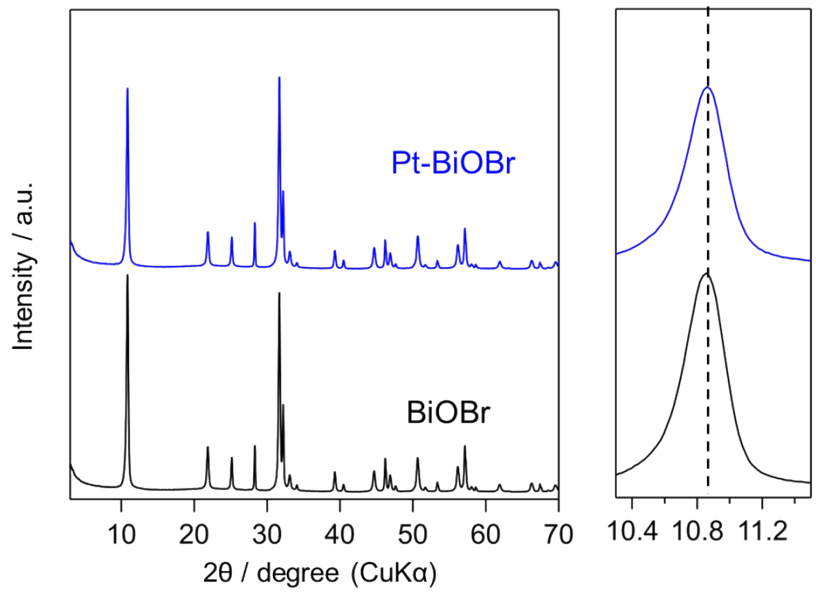

Figure S5. XRD patterns of BiOBr and Pt-BiOBr.

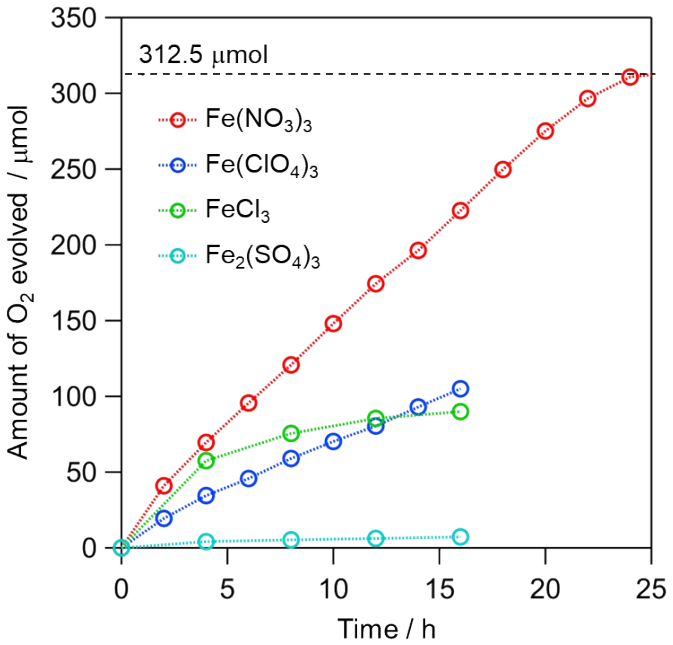

Figure S6. Time courses of O_2 evolution over unmodified BiOBr from aqueous Fe^{3+} solution (5 mM, 250 mL) with various counter anions (NO_3^-, ClO_4^-, Cl^-, or SO_4^{2-}) under UV–visible light irradiation ($\lambda > 300$ nm).

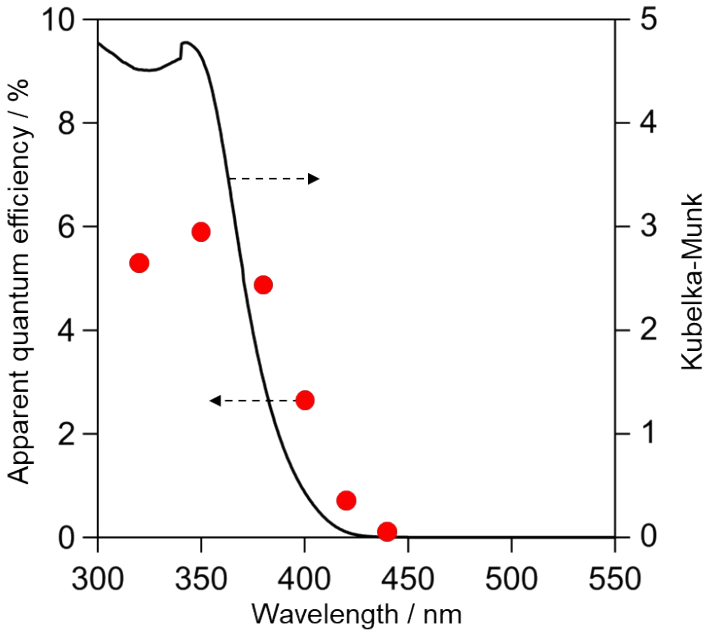

Figure S7. Apparent quantum efficiency of Pt-BiOBr for O_2 evolution from aqueous $Fe(NO_3)_3$ solutions under monochromatic light irradiation.

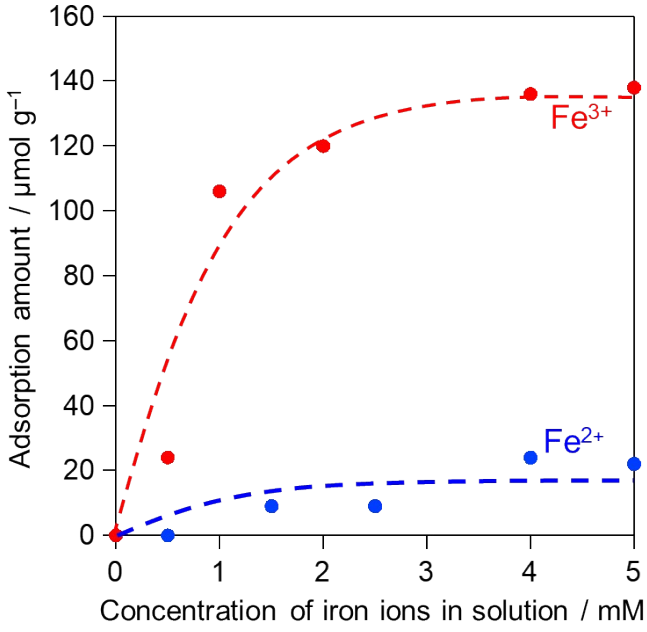

Figure S8. Adsorption properties of iron cations (Fe^{2+} and Fe^{3+}) on BiOBr (counter anion: ClO_4^-).

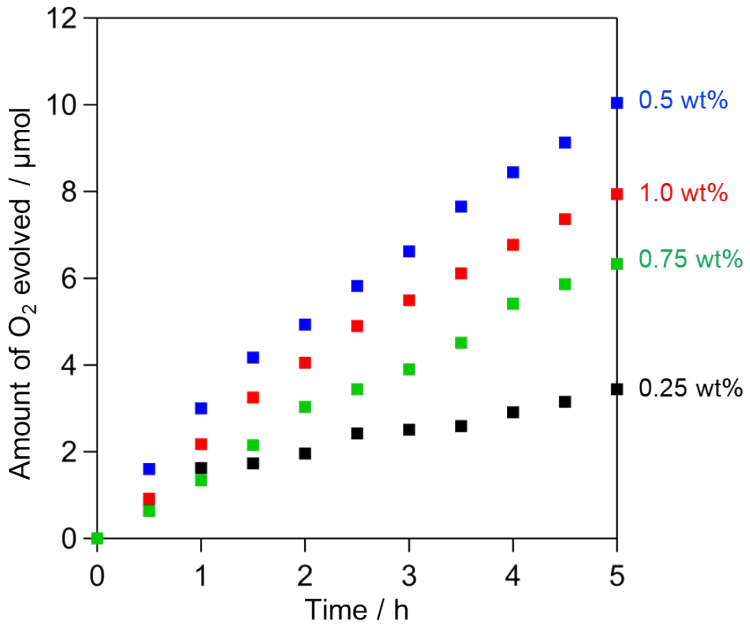

Figure S9. Time courses of O_2 evolution over Pt-$BiOBr_{1-x}I_x$ with different Pt loadings (0.25, 0.5, 0.75, and 1.0 wt%) from an aqueous $Fe(NO_3)_3$ solution (1 mM, 250 mL) under visible light (λ > 400 nm).

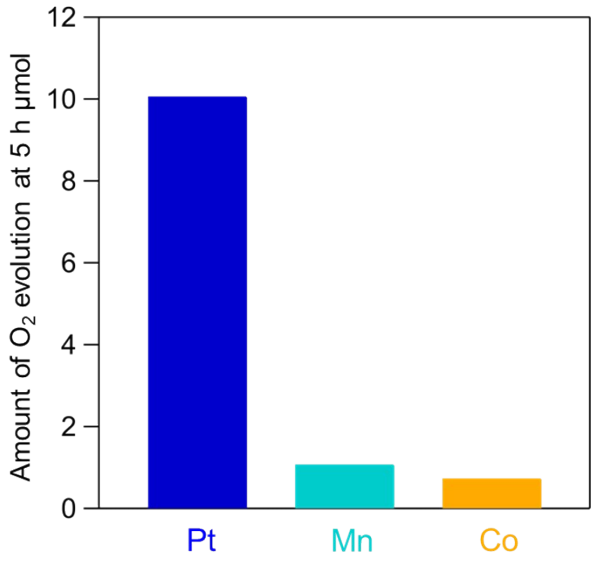

Figure S10. Photocatalytic O_2 evolution amounts over $BiOBr_{0.9}I_{0.1}$ loaded with different cocatalysts (Pt, Mn, and Co species) from an aqueous $Fe(NO_3)_3$ solution (1 mM, 250 mL) under visible light (λ > 400 nm). Mn and Co species were loaded by the impregnation method (0.5 wt% as metal) using $Co(NO_3)_2 \cdot 6H_2O$ and $Mn(NO_3)_2 \cdot 6H_2O$ as precursors, respectively, followed by calcination in air at 350 °C for 1 h.

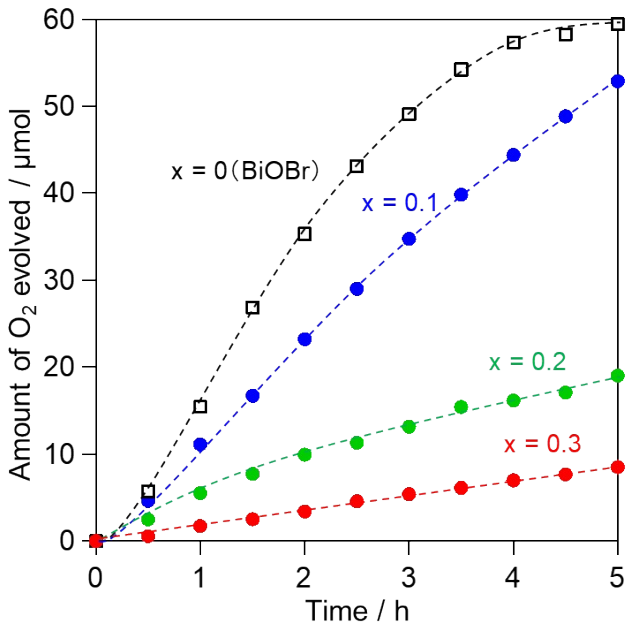

Figure S11. Time courses of O_2 evolution over Pt-$BiOBr_{1-x}I_x$ from aqueous $Fe(NO_3)_3$ solution (1 mM, 250 mL) under UV–visible light ($\lambda > 300$ nm).

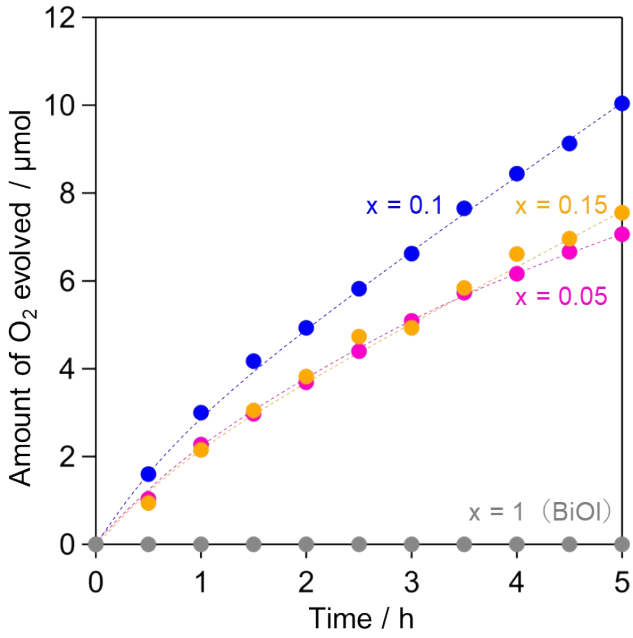

Figure S12. Time course of O_2 evolution over Pt-$BiOBr_{1-x}I_x$ (x = 0.05, 0.1, 0.15, and 1) from an aqueous $Fe(NO_3)_3$ solution (1 mM, 250 mL) under visible light ($\lambda > 400$ nm).

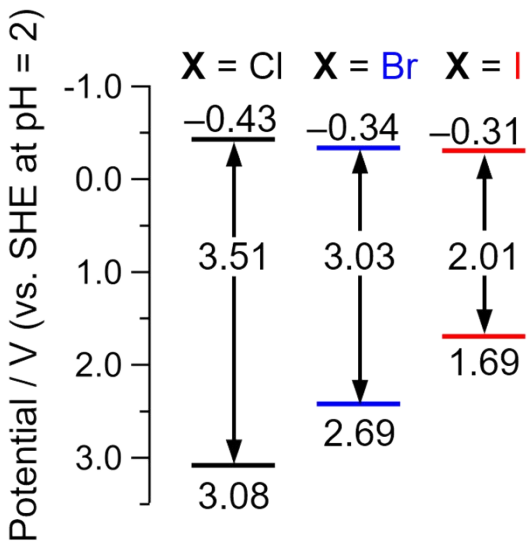

Figure S13. Band levels of BiOX estimated from the diffuse reflectance spectra and Mott–Schottky plots. This figure is reproduced from *Phys. Chem. Chem. Phys.*, 2026, **28**, 38–41.

Table S2. Full width at half-maximum (FWHM) and crystallite sizes for the (001) and (102) peaks in the XRD patterns of $BiOBr_{1-x}I_x$ (x = 0–0.3).

x	FWHM (001) (deg.)	Crystallite size[a] (001) (Å)	FWHM (102) (deg.)	Crystallite size[a] (102) (Å)
0	0.332	251	0.268	322
0.1	0.449	186	0.370	233
0.2	0.471	177	0.523	165
0.3	0.561	149	0.697	124

[a]Crystallite sizes were estimated using the Scherrer equation.

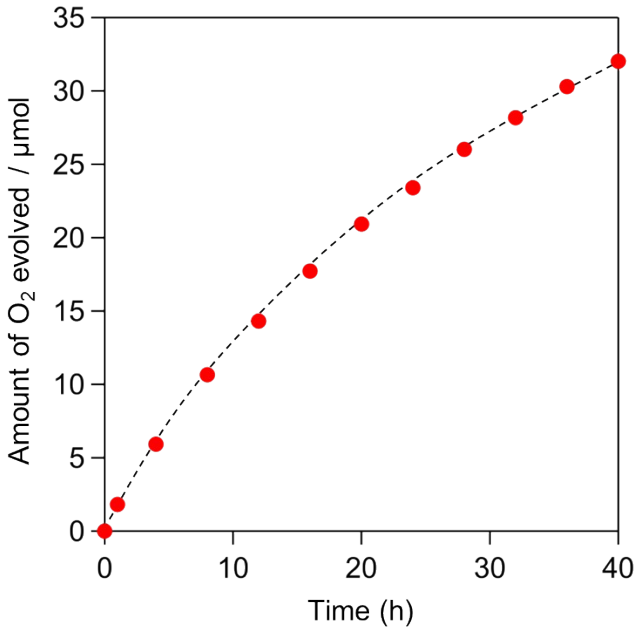

Figure S14. Time courses of O_2 evolution over Pt-$BiOBr_{0.9}I_{0.1}$ from aqueous $Fe(NO_3)_3$ solution (1 mM, 250 mL) under visible light ($\lambda > 400$ nm) during a prolonged reaction period.

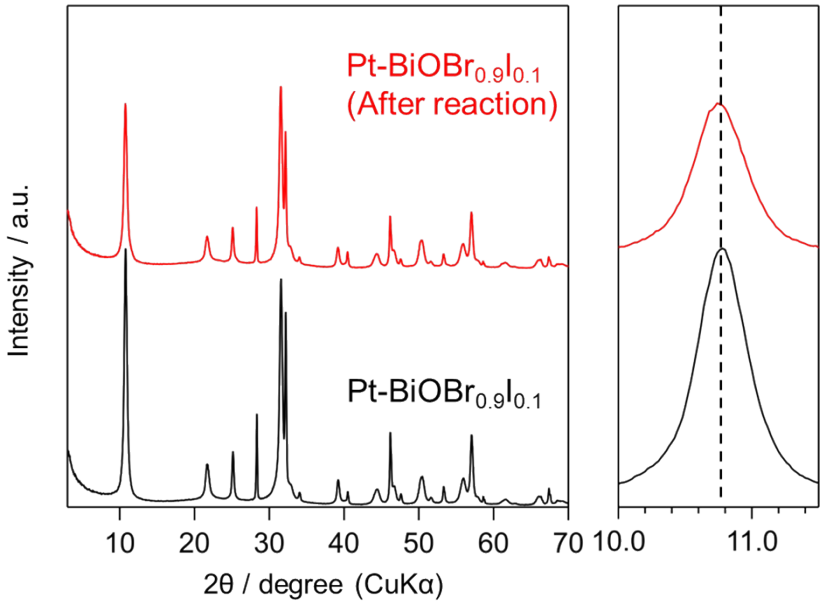

Figure S15. XRD pattern of Pt-$BiOBr_{0.9}I_{0.1}$ before and after long-term photocatalytic O_2 evolution (Figure S14) under visible-light irradiation ($\lambda > 400$ nm).

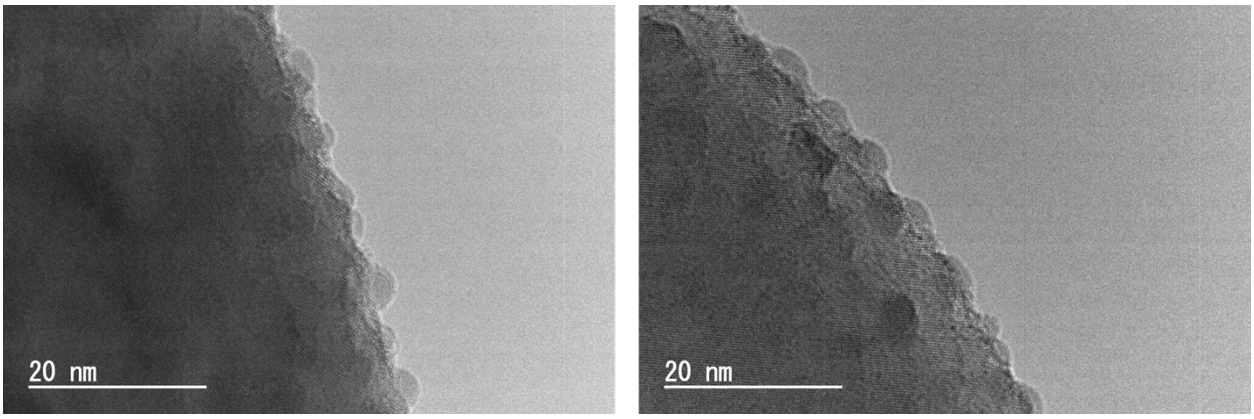

Figure S16. TEM image of Pt-$BiOBr_{0.9}I_{0.1}$ via the arc plasma method.

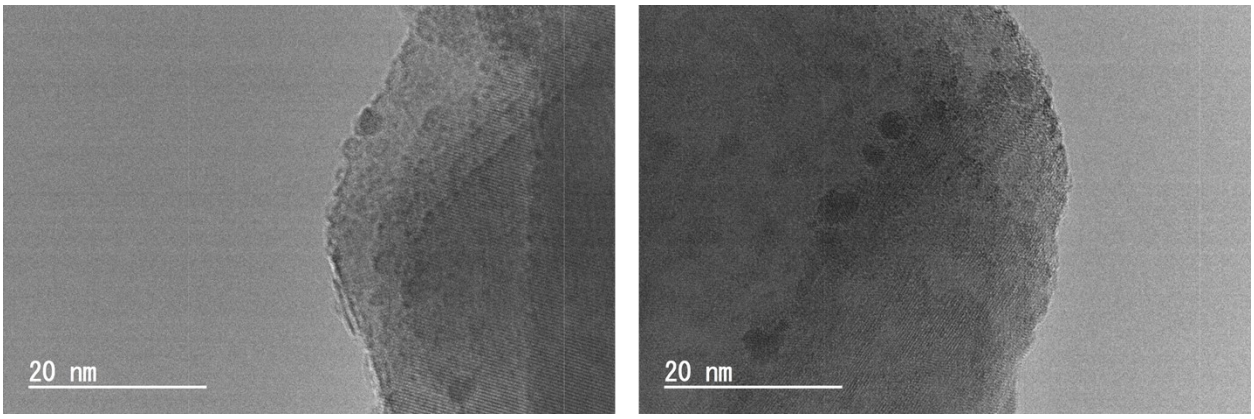

Figure S17. TEM image of Pt-$BiOBr_{0.9}I_{0.1}$ via the impregnation method.

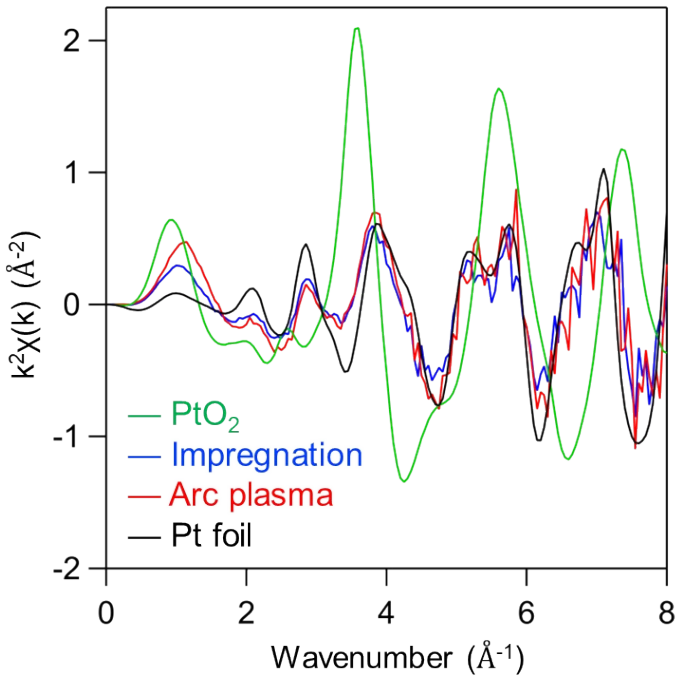

Figure S18. Pt L_3-edge EXAFS $k^2\chi(k)$ function for Pt-$BiOBr_{0.9}I_{0.1}$ prepared by arc-plasma and impregnation methods, along with those of Pt foil and PtO_2 as references.

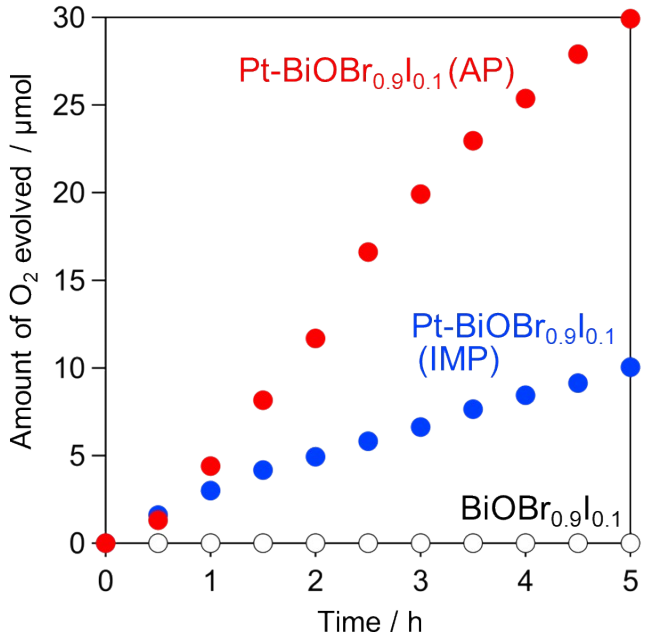

Figure S19. Time courses of O_2 evolution over $BiOBr_{0.9}I_{0.1}$ or Pt-$BiOBr_{0.9}I_{0.1}$ prepared by arc plasma (AP) or impregnation (IMP) methods from aqueous $Fe(NO_3)_3$ solution (1 mM) under visible-light irradiation ($\lambda > 400$ nm).

Table S3. EDX-determined I/(Br + I) and I/Bi ratios of Pt-$BiOBr_{0.9}I_{0.1}$ (AP) before and after the O_2 evolution.

	I/(Br+I)	I/Bi
$BiOBr_{0.9}I_{0.1}$	0.11	0.11
Pt-$BiOBr_{0.9}I_{0.1}$ (AP) after the O_2 evolution	0.12	0.12

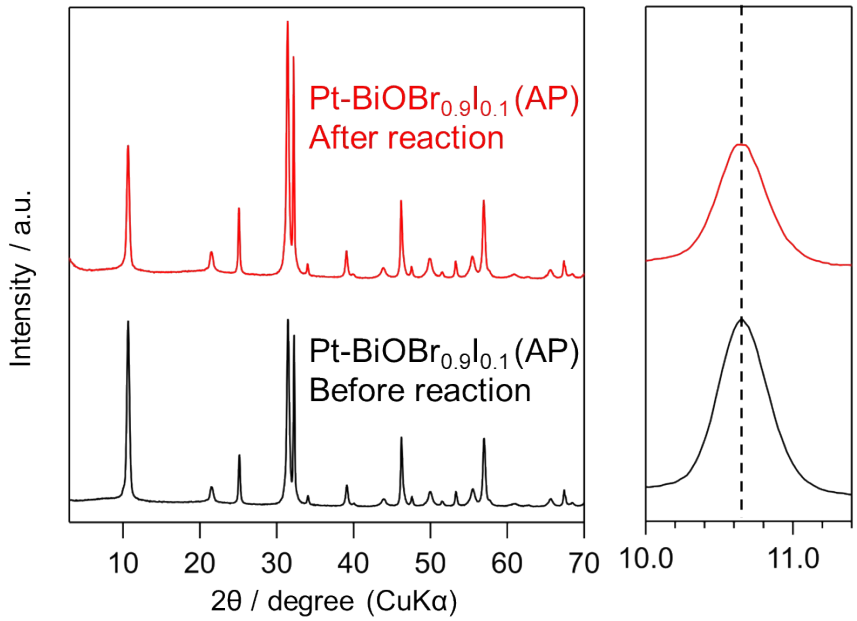

Figure S20. XRD pattern of Pt-$BiOBr_{0.9}I_{0.1}$ prepared by arc-plasma (AP) after photocatalytic O_2 evolution under visible light irradiation (λ > 400 nm). The data were collected using a MiniFlex 600-C diffractometer (Rigaku Corp.) with Cu Kα radiation.

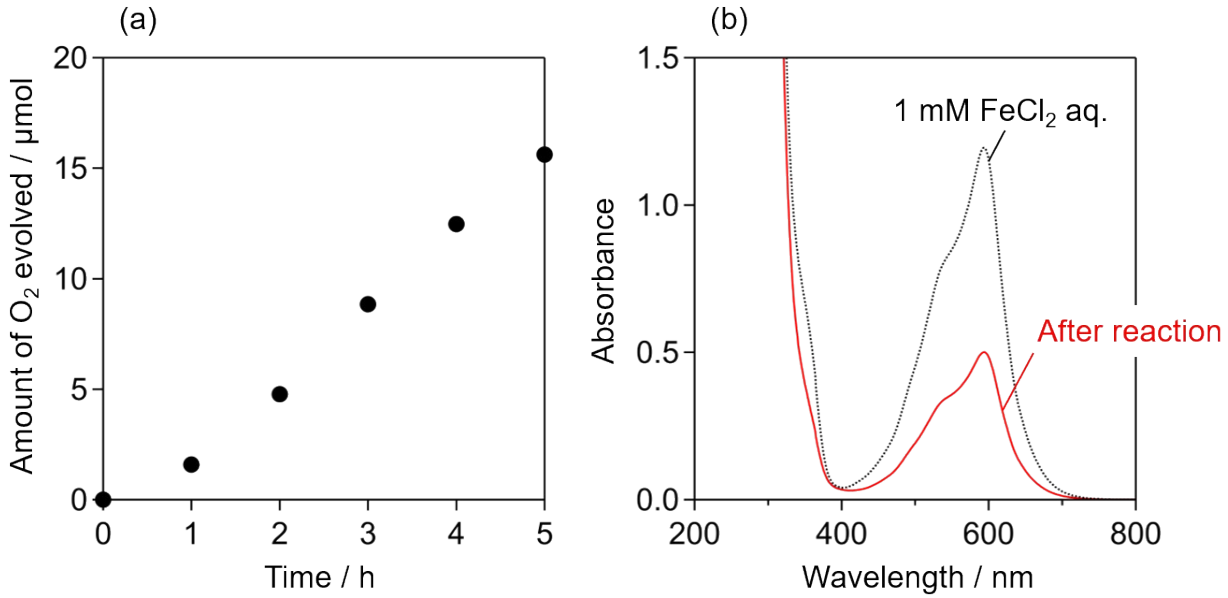

Figure S21. (a) Time courses of O_2 evolution over Pt-$BiOBr_{0.9}I_{0.1}$ (AP) from aqueous $Fe(NO_3)_3$ solution (1 mM) under visible-light irradiation (λ > 400 nm). (b) Absorption spectra of aqueous solutions in the presence of Fe^{2+} after the photocatalytic reaction; Fe^{2+} is detected as Fe^{2+}–2,4,6-tris(2-pyridyl)-1,3,5-triazine (TPTZ) complex (see *J. Am. Chem. Soc.* 2021, **143**, 8446–8453). The amount of evolved O_2 and generated Fe^{2+} after 5 h of irradiation was estimated to be 16 and 60 μmol, respectively, which are in reasonable agreement considering the four-electron nature of water oxidation.

Table S4. Comparison of apparent quantum efficiency (AQE) of photocatalytic O_2 evolution in the presence of Fe^{3+} electron acceptors on various Sillén-type oxyhalide photocatalysts.

Photocatalyst	Wavelength	Electron acceptor	Cocatalyst	AQE (%)	Ref.
$PbBiO_2Cl$	400 nm	$Fe(NO)_3$	RuO_2	0.9	(1)
$PbBi_3O_4Cl_3$	400 nm	$Fe(ClO_4)_3$	RuO_x	1.9	(2)
$SrBi_3O_4Cl_3$	420 nm	$Fe_2(SO_4)_3$ $FeCl_3$	RuO_2	0.3 0.9	(3)
$BiOBr_{0.9}I_{0.1}$	405 nm	$Fe(NO)_3$	Pt	0.7	This work

Reference
(1) *Chem. Mater.* 2018, **30**, 5862–5869.
(2) *Chem. Mater.* 2021, **33**, 9580-9587.
(3) *J. Mater. Chem. A*, 2023, **11**, 15159-15167.

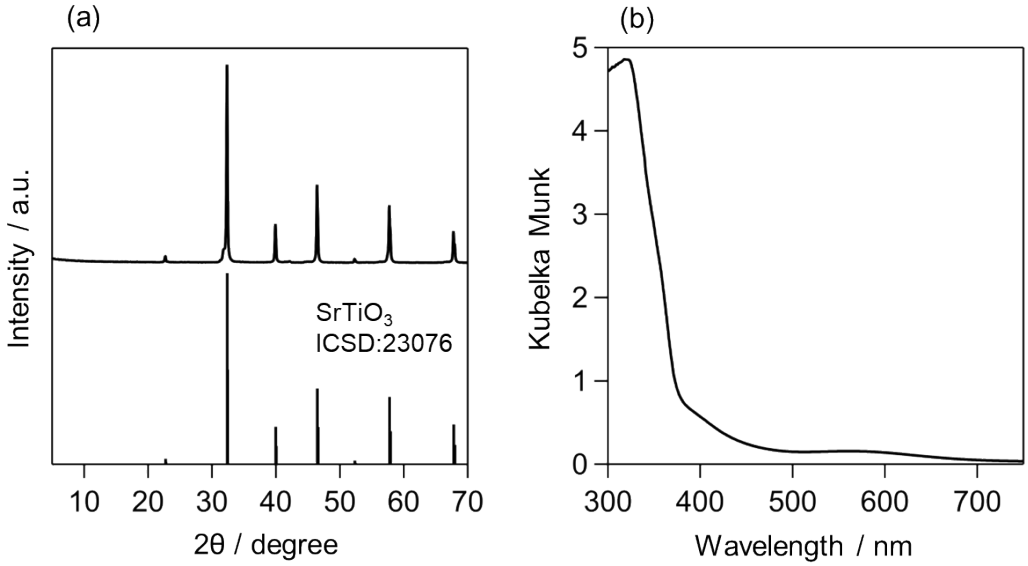

Figure S22. (a) XRD pattern and (b) UV–vis diffuse reflectance spectrum of $SrTiO_3$:Rh.

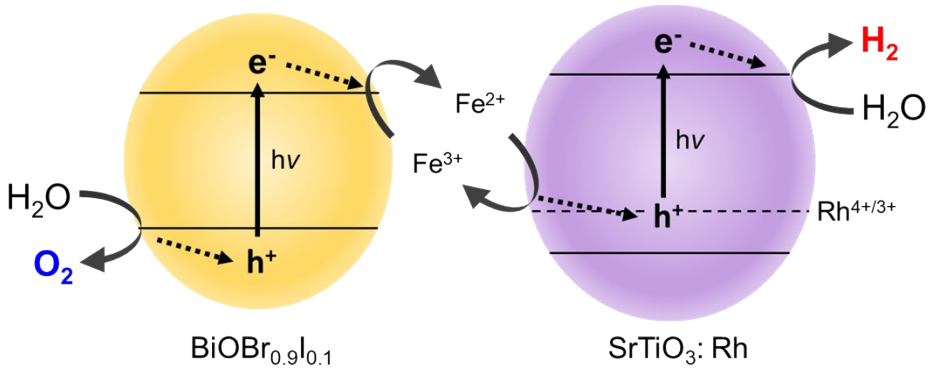

Figure S23. Schematic of Z-scheme water splitting using a mixture of Ru-loaded $SrTiO_3$:Rh as a H_2-evolution photocatalyst and Pt-$BiOBr_{0.9}I_{0.1}$ (AP) as an O_2-evolution photocatalyst in the presence of an Fe^{3+}/Fe^{2+} redox mediator.